Journal of Materials Chemistry C

ROYAL SOCIETY OF CHEMISTRY

PAPER

View Article Online
View Journal | View Issue

Cite this: J. Mater. Chem. C, 2025, 13, 11879

Covalent carbon nanodot-azobenzene hybrid photoswitches: the impact of *meta*/*para* connectivity and sp^3 spacer on photophysical properties†

Paul P. Debes, ‡[ab] Dominic Schatz, ‡[ac] Yagmur Aydogan-Sun, [d] Juan Pablo Martínez, [e] Michal Langer, [f] Janis Hessling, [g] Jaime Gallego, [ab] Enzo Menna, [h] Bernd M. Smarsly, [ab] Monika Schönhoff, [g] Silvio Osella, [e] Josef Wachtveitl, [d] Hermann A. Wegner *[ac] and Teresa Gatti *[abi]

The covalent surface functionalization of carbon nanodots (**CNDs**) can facilitate the design and development of nanocarbon hybrids with photoswitching properties, which can be applied in a wide range of applications, including sensing, optoelectronics, and even bio-applications. This study underscores the potential utilization of these hybrids as photoresponsive materials, for potential application in optostimulation. In this study, we examine the characteristics of covalent azobenzene-functionalized **CNDs**, with a particular emphasis on the impact of *meta* and *para* connectivity and the additional introduction of a glycine spacer. The **CND** synthesis process comprises a bottom-up microwave condensation of ethylenediamine and citric acid. Amide coupling to azobenzenes is confirmed through NMR diffusion-ordered spectroscopy and diffusion decay analysis. A comprehensive investigation is conducted into the size and optical properties of the resulting hybrids. Moreover, time-dependent density functional theory computations are employed to understand absorption spectra and charge transfer events. Furthermore, advanced optical characterisation is utilised to examine energy/charge transfer between the constituents. Finally, the switching properties, fatigue resistance, and half-life of the hybrids are studied to evaluate their performance for prospective applications like in optostimulation.

Received 10th January 2025,
Accepted 6th May 2025

DOI: 10.1039/d5tc00116a

rsc.li/materials-c

Introduction

The field of optostimulation is receiving increased attention due to its potential to enable remote monitoring of cellular signaling with high precision.[1] Furthermore, the utilization of nanoparticles for biomedical applications is an expanding area of research, with the primary objectives of enhancing imaging techniques and improving drug delivery systems.[2] Both approaches serve as valuable tools for advancing our understanding of bacterial cell physiology in both fundamental and applied research contexts. In 2023, the group of Paternò demonstrated that an amphiphilic azobenzene (azo) unit can non-covalently attach to the plasma membrane of *Bacillus subtilis* bacteria.[3] Upon irradiation and azo isomerization, the membrane structure relaxes and expands. It has been demonstrated that carbon nanodots (**CNDs**) are capable of localizing within biomembranes. Consequently, covalent functionalization of **CNDs** with azos could enable the development of a hybrid material capable of entering biomembranes, being sensed, and undergoing structural changes in response to light

[a] Center for Materials Research, Justus Liebig University, Heinrich-Buff-Ring 16, 35392, Giessen, Germany
[b] Institute of Physical Chemistry, Justus Liebig University, Heinrich-Buff-Ring 17, 35392, Giessen, Germany
[c] Institute of Organic Chemistry, Justus Liebig University, Heinrich-Buff-Ring 17, 35392, Giessen, Germany. E-mail: Hermann.A.Wegner@org.chemie.uni-giessen.de
[d] Institute of Physical and Theoretical Chemistry, Goethe University, Max von Laue-Strasse 7, 60438, Frankfurt, Germany
[e] Chemical and Biological Systems Simulation Lab, Centre of New Technologies, University of Warsaw, 2c Banacha Street, 02-097, Warszawa, Poland
[f] IT4Innovations, VSB – Technical University of Ostrava, 17.listopadu 2172/15, 70800, Ostrava-Poruba, Czech Republic
[g] Institute of Physical Chemistry, University of Muenster, Corrensstrasse 28/30, 48149, Muenster, Germany
[h] Department of Chemical Sciences, University of Padova and INSTM UdR Padova, via Marzolo 1, 35131, Padova, Italy
[i] Department of Applied Science and Technology, Politecnico di Torino, C.so Duca degli Abruzzi 24, 10129, Torino, Italy. E-mail: teresa.gatti@polito.it

† Electronic supplementary information (ESI) available. See DOI: https://doi.org/10.1039/d5tc00116a

‡ These authors contributed equally.

irradiation.[4,5] Ultimately, this research aims to provide new tools for effective optostimulation and imaging applications in biomedical research.

Combining different materials not only improves functionality, but also results in a wide range of properties that can be tailored for specific applications in microbial systems and beyond. Over the past decade, the field of carbon nanomaterials has witnessed a growing body of research. Fullerenes, **CNDs**, carbon nanotubes, and graphene are prominent examples of these carbon nanomaterials.[6–10] Notably, **CNDs** have attracted attention due to their facile synthesis, low cost, excellent biocompatibility, easy functionalization, water solubility, and bright luminescence.[11] Bottom-up **CNDs** are synthesized using small molecules as starting materials.[12] Commonly utilized molecules for synthesis include citric acid (CA), urea, amino acids, and ethylene diamine (EDA). The resulting nanoparticles exhibit a quasi-spherical shape and are typically smaller than 10 nm in size.[13] These nanoparticles consist of carbon, hydrogen, oxygen, and often nitrogen.[14] **CNDs** are composed of a carbon core surrounded by functional groups.[15] The type and quantity of functional groups on the surface of **CNDs** are influenced by the selected starting materials and their ratios.[16] Alcohols, amines, and carboxylic acids are common functional groups that allow covalent functionalization of a wide range of materials.[17,18] Among the innumerable possibilities, functionalization with photochromic molecules enables the production of carbon nanomaterials with the ability to respond to light irradiation.[19] Photoswitchable molecules have the capability to undergo a light-induced reversible transformation from one species to another. Depending on the molecule, there are at least two states which are stable or metastable.[20]

One of the widely used photochromic motifs is the *trans*/*cis* isomerization of azos,[21,22] stilbenes,[23] hydrazones,[24–26] and Schiff bases.[27,28] Azos undergo a significant change in length and geometry through isomerization, making them useful in energy or information storage,[29–34] photobiology,[35,36] host–guest systems,[37] as molecular wind-up meters,[38] and molecular machines.[39,40] The *trans* to *cis* isomer switch is usually induced by irradiation in the π–π* band, typically between 300 nm and 360 nm. Reversion to the thermodynamically favored *trans* isomer can be induced thermally or by n–π* excitation around 440 nm,[40,41] or by various catalytic processes.[42,43] The linkage of two azo units, either *via* the *para* or the *meta* position, has demonstrated that the resulting combinations exhibit distinct properties. Compared to the π-conjugation in the *para*-connected azo, the *meta*-connection resulted in a more independent behavior of the two entities.[44–46] Even if the systems are separated through space and are not in conjugation with each other, they influence one another.[47,48] For a better understanding of the connectivity and through-space interaction between azos and nanocarbons such as **CNDs**, we report in this work three different systems with either *meta*- or *para*-connectivity, and considering a sp^3 spacer between the two moieties in one of the systems. The impact of functionalization type and inter-unit distance on physicochemical characteristics—specifically absorbance, photoluminescence (PL), quantum yield (QY), half-life, and fatigue resistance—has been comprehensively investigated. Moreover, time-correlated single photon counting (TCSPC) is utilized to investigate the energy/charge transfer occurring between these components. Additionally, theoretical analysis of absorbance properties was conducted using time-dependent density functional theory (TDDFT) computations to provide deeper insights.

These different **CND–azo** hybrids could serve as valuable platform for functional species in several light-triggered applications.

Results and discussion

CNDs were synthesized *via* a microwave (MW)-assisted reaction between CA and EDA in a 1 : 1 ratio, followed by purification through filtration and dialysis. The synthesized **CNDs** were thoroughly characterized using atomic force microscopy (AFM), UV-vis absorbance, PL, and NMR spectroscopy to confirm their presence and gain insight into their properties. In a previous study, we reported the presence of **CNDs** featuring surface-exposed primary amine groups, which are available for further functionalization *via* an amide coupling reaction.[16] Three distinct azo derivatives were synthesized utilizing the Baeyer–Mills reaction, each containing a carboxylic acid functional group. The first derivative has *meta* (***m***) connectivity, the second has *para* (***p***) connectivity, and the third has a glycine spacer in the *meta* position (***m*-Gly-Azo**). Subsequently, the azo compounds were covalently bonded to the **CNDs** *via* an amide coupling, as illustrated in Fig. 1. To provide comprehensive evidence of the successful functionalization of the **CND** with the respective azo diffusion-ordered spectroscopy (DOSY) NMR was used. A similar approach was employed in 2018 by Prato and co-workers to demonstrate covalent functionalization of **CNDs**.[49] Bare ***m*-Azo**, pristine **CND**, a physical mixture of **CND** and ***m*-Azo**, and the three hybrids were subjected to 2D DOSY NMR (see Fig. S1 to S6, ESI†) as well as an analysis of the diffusion decays (see Fig. 2). In the DOSY spectra ***m*-Azo**, **CND**, and the hybrids exhibit a single monomodal distribution, indicating that the constituents of these samples are present in a monodispersed state. In contrast, the physical mixture of **CND** and azo shows two separate diffusion distributions, which proves that the two moieties move separately in the mixture. For a more precise quantification, the diffusion coefficients were derived from the diffusion echo decays (see Fig. 2A) by applying the Stejskal–Tanner equation,[50] and assuming a log-normal distribution of the diffusion coefficients (see ESI,† eqn (S2) and (S3)).

Since no separate ***m*-Azo** resonances could be identified in the hybrid samples (see Fig. S1–S6, ESI†), the integral over the chemical shift region from 8.5 to 7.3 ppm was evaluated in all cases. ***m*-Azo** was used as a representative Azo moiety to compare the molecular diffusion coefficients to those of **CND** and the hybrids. The diffusion coefficient of ***m*-Azo** in solution is depicted as a dotted red line at 2.93×10^{-10} m^2 s^{-1}, as it does not possess a size distribution, in contrast to the **CND** or the hybrids (Fig. 2B). The diffusion coefficient distribution for pristine **CND** exhibits a maximum at $D = 1.05 \times 10^{-10}$ m^2 s^{-1}.

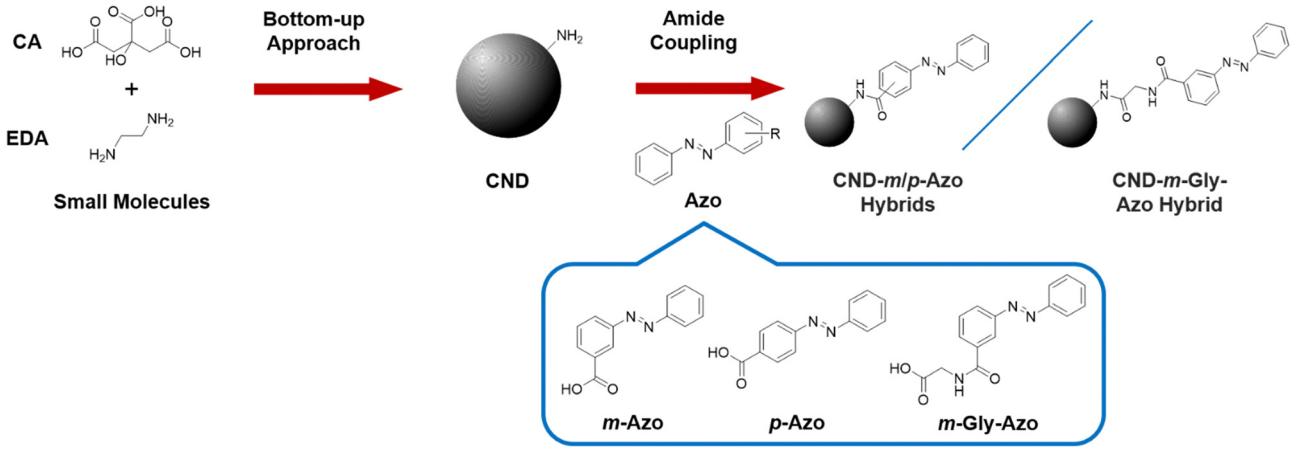

Fig. 1 Schematic representation of the microwave-assisted bottom-up synthesis of the **CND** from CA and EDA (1 : 1) in aqueous solution, followed by the covalent functionalization *via* amide coupling (EDC, NHS in DMF) with three different azos (***m*-Azo**, ***p*-Azo**, and ***m*-Gly-Azo**) forming three distinct **CND–azo** hybrids, namely: **CND–*m*-Azo**, **CND–*p*-Azo**, and **CND–*m*-Gly-Azo**.

Measurements of the hybrids revealed a 20% reduction in the diffusion coefficient, with values of 0.84×10^{-10} m^2 s^{-1} observed for both the **CND–*m*-Azo** and the **CND–*m*-Gly-Azo** hybrids. The **CND–*p*-Azo** hybrid exhibited a diffusion coefficient of 0.93×10^{-10} m^2 s^{-1}, which corresponds to a decrease of 11% in comparison to pristine **CND**. A decrease of the diffusion coefficients accompanies an increase in particle size, which is consistent with successful functionalization of the **CNDs**. In contrast, the physical mixture of **CNDs** with ***m*-Azo** shows two independent peaks in the diffusion domain of the 2D spectrum (Fig. S3, ESI†), which can be viewed as separate peaks in the distribution of diffusion coefficients in Fig. 2B. Notably, the fast-diffusing component, attributed to ***m*-Azo**, exhibits a slightly slower diffusion in the presence of **CNDs** as compared to bare ***m*-Azo** solution, but generally agrees with the diffusion coefficient of bare ***m*-Azo**. Furthermore, the diffusion coefficient of the **CNDs** in the mixture, represented by the shoulder with the lower diffusion coefficient, agrees very well to that of bare **CND**. This indicates that the physical mixture consists of ***m*-Azo** and **CND** as distinct species. In contrast, the hybrid samples do not exhibit any component with a fast diffusion coefficient, suggesting the absence of individual ***m*-Azo** molecules. Additionally, the reduced diffusion of the hybrid **CND** particles reflects an increased radius, consistent with functionalization. In consideration of the Stokes–Einstein equation (see ESI,† eqn (S4)), the hydrodynamic diameter can be determined from the diffusion coefficient at the maximum. The size of the **CND** is at around 1.9 nm and the **CND–*m*-Azo** at around 2.4 nm, which is in good

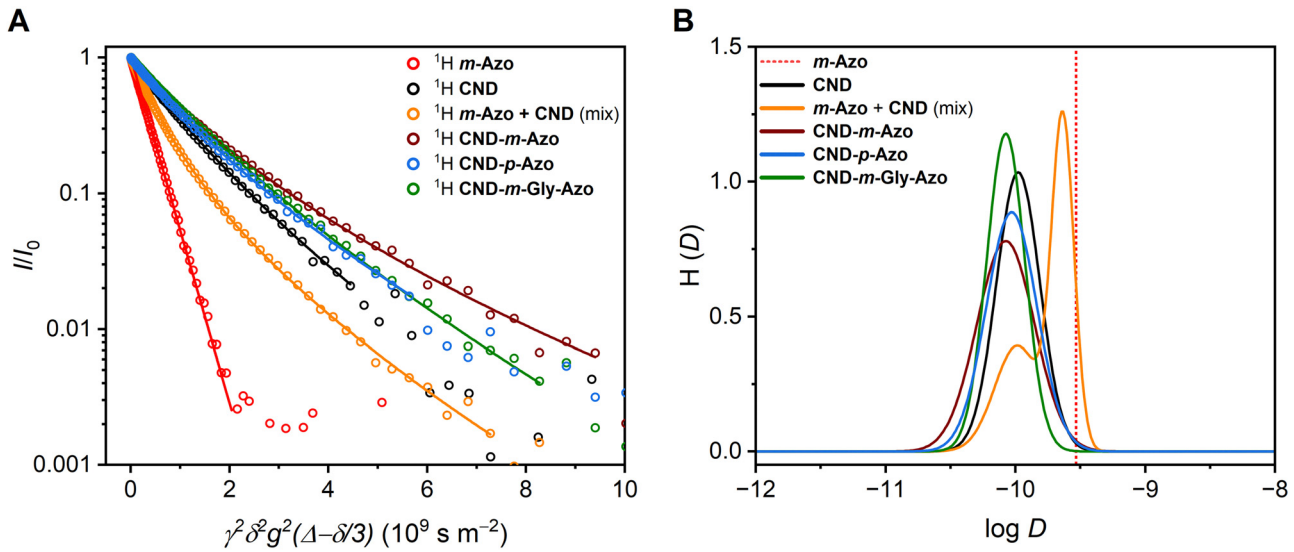

Fig. 2 (A) ^{1}H diffusion decay signal, integrated from 8.5 ppm to 7.3 ppm for the ***m*-Azo**, **CND**, a physical mixture of ***m*-Azo** and **CND** (1 : 10), **CND–*m*-Azo**, **CND–*p*-Azo**, and **CND–*m*-Gly-Azo** hybrids. (B) Distribution of diffusion coefficients according to the method of Lenoch *et al.*[27] (see description in ESI†) for ***m*-Azo**, **CND**, a physical mixture of ***m*-Azo** and **CND** (1 : 10), **CND–*m*-Azo**, **CND–*p*-Azo**, and the **CND–*m*-Gly-Azo**. The diffusion coefficient of ***m*-Azo** is depicted as straight dotted line due to lack of a size distribution.

Table 1 The maximum of the diffusion coefficient distribution, derived from fitting of echo decays. Moreover, the hydrodynamic diameter, calculated using the Stokes–Einstein equation

Sample	D/m^2 s^{-1}	Hydrodynamic diameter/nm
***m*-Azo**	2.93×10^{-10}	0.68
CND	1.05×10^{-10}	1.90
***m*-Azo** + **CND** (physical mix)[a]	2.32×10^{-10}	0.86
	1.03×10^{-10}	1.90
CND–*m*-Azo	0.84×10^{-10}	2.40
CND–*p*-Azo	0.93×10^{-10}	2.10
CND–*m*-Gly-Azo	0.84×10^{-10}	2.40

[a] The physical mixture corresponds to a weight ratio of 1 : 10 of ***m*-Azo** to **CND**.

Table 2 UV-vis absorption maxima (λ_{Abs}), PL maxima (λ_{Em}), Stokes shift, and PLQY of the three **CND–azo** hybrids compared to pristine **CNDs**, pristine azos, and physical mixtures of the azos and the **CNDs**

Sample	λ_{Abs}/nm	λ_{Em}/nm	Stokes shift/nm	PLQY/%
***m*-Azo**	326			
***p*-Azo**	335			
***m*-Gly-Azo**	323			
CND	357	443	86	37
CND–*m*-Azo	350	440	90	18
CND–*p*-Azo	349	443	94	11
CND–*m*-Gly-Azo	329	441	112	1
CND + ***m*-Azo** (mix)	349	443	94	31
CND + ***p*-Azo** (mix)	343	443	100	18
CND + ***m*-Gly-Azo** (mix)	338	443	105	23

agreement with the measured AFM size (see Fig. S7, S8, and S11A and B, ESI†). Accordingly, the size of the remaining hybrids can be given by the hydrodynamic diameter as well. **CND–*p*-Azo** possess a size of 2.1 nm, while the **CND–*m*-Gly-Azo** measures 2.4 nm (Table 1). Whereas AFM measurements indicate a size of 4.9 nm for the **CND–*p*-Azo** and 4.8 nm for the **CND–*m*-Gly-Azo**, which can be attributed to potential agglomerates on the mica surface (see Fig. S9, S10, and S11C and D, ESI†).[51]

Thermogravimetric analysis (TGA) suggests the occurrence of functionalization; however, the **CND** morphology precludes the possibility of making a precise statement regarding the degree of functionalization based on TGA results (Fig. S12, ESI†). As illustrated in Fig. 3, the absorption and emission spectra of the three hybrids are displayed in comparison to the pristine **CND** and the absorption of the corresponding azo compound (which are non-emissive). Table 2 presents the individual maxima of the absorption λ_{Abs} and emission λ_{Em}, the Stokes shift, as well as the PLQY (Fig. S13 and S14, ESI†).

A comparative analysis of the absorption spectra of the three hybrids revealed that **CND–*m*-Azo** exhibited the smallest blue shift compared to the **CND**, with an absorption maximum at 350 nm *versus* 357 nm for **CND**. In contrast, **CND–*m*-Gly-Azo** displayed the largest blue shift (maximum at 329 nm), while **CND–*p*-Azo** (maximum at 349 nm) showed a shift similar to that of **CND–*m*-Azo**. Qualitative analysis of the ^{1}H NMR spectra indicates that **CND–*m*-Gly-Azo** has a greater quantity of ***m*-Gly-Azo** on its surface, as evidenced by more pronounced azo group peaks compared to **CND–*m*-Azo** and **CND–*p*-Azo** (Fig. S57–S59, ESI†). This finding suggests that the extent of functionalization significantly influences the observed shifts of the absorption maxima. Although **CND–*p*-Azo** and **CND–*m*-Azo** exhibit comparable blue shifts relative to pure **CND**, ***p*-Azo** shows a larger red shift (335 nm) than ***m*-Azo** (323 nm), contributing to the minor blue shift in **CND–*p*-Azo**. To quantify surface functionalization, UV-vis spectra were deconvoluted using two Lorentzian functions, allowing for calculation of azo concentrations *via* Beer–Lambert law.[52] The absorbance coefficients of the azo groups were considered (Fig. S15, ESI†), along with the maximum absorbance values derived from the deconvolution, which represent the respective azo species (Fig. S16, ESI†). This methodology has already been applied in a similar way to functionalized **CNDs** in one of our previous studies.[53] The azo content was found to be 3.4% by mass for **CND–*m*-Azo** and 4.5% for **CND–*p*-Azo**, while **CND–*m*-Gly-Azo** exhibited a significantly higher value of 24%. Corresponding primary amine amounts were calculated as 150 μmol g^{-1} for **CND–*m*-Azo**, 200 μmol g^{-1} for **CND–*p*-Azo**, and 850 μmol g^{-1} for **CND–*m*-Gly-Azo**, consistent with previous findings on amine functionalization on these **CNDs**. In a previous study, the maximum amount of primary amines measured on the surface of the **CND**

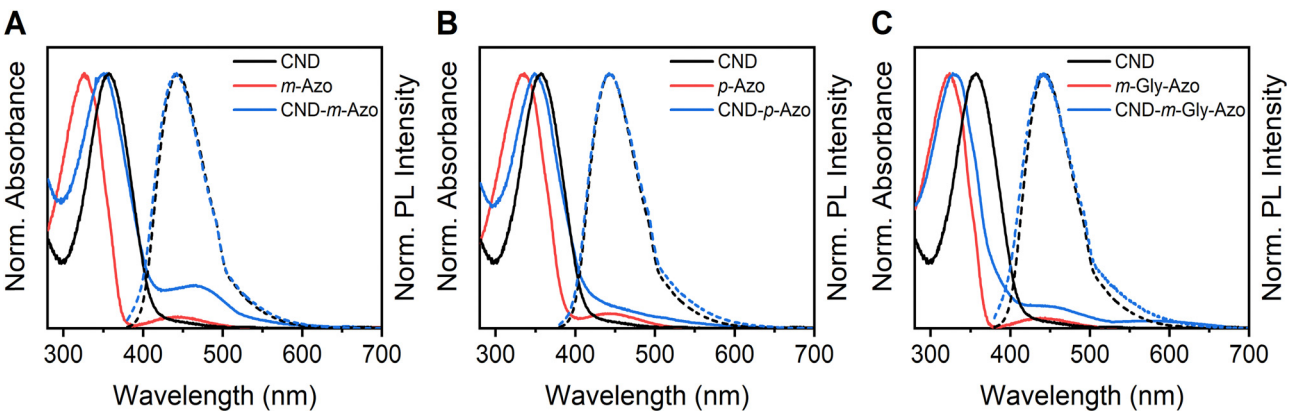

Fig. 3 Normalized absorbance (red solid lines) of (A) ***m*-Azo**, (B) ***p*-Azo**, (C) ***m*-Gly-Azo**, normalized absorbance (blue solid lines) and PL (blue dotted lines) of (A) **CND–*m*-Azo**, (B) **CND–*p*-Azo**, (C) **CND–*m*-Gly-Azo** compared to pristine **CNDs**.

was measured to be 1670 μmol g^{-1}.[16] It is a well-known phenomenon that complete functionalization of primary amines on the **CND**'s surface is rarely achieved. However, to increase the degree of functionalization, it is possible to change the starting materials of the **CND** to more nitrogen-rich precursors, such as arginine, or to increase the EDA content to obtain a larger amount of primary amines on the surface of the **CND**.[54]

The degree of azo functionality on the surface of the **CNDs** may be influenced by the nature of the established connectivity. Preliminary observations suggest that ***m*-Azo** may exhibit greater steric demand compared to ***p*-Azo**; however, this assertion requires further investigation. In contrast, the introduction of a glycine spacer appears to reduce this steric demand, thereby facilitating a higher degree of functionalization within the *meta*-connected hybrids. This indicates that the connectivity and spacer design can modulate the optical properties. *Meta*-Functionalization is expected to lead to a more independent behavior of the **CND** and azo, while *para* connectivity may allow conjugation between the two systems.[15,44] As a matter of fact, the hybrids exhibited frontier molecular orbitals localized on either the **CND** or azo fragments, but the conjugation is not extended on both (Fig. 4). Although *para*-functionalization should enable conjugation and thus strong intramolecular interaction, this is not evident in the absorption spectra. This implies that the azo moiety remains spatially separated from the fluorophores of the **CND** and only engages through space.

Computational investigations were further employed to understand the UV-vis spectra presented in Fig. 3. First, molecular dynamics (MD) simulations were performed to develop a thermally stable model representing the molecular structure of the **CND** (Fig. S17 and S20, ESI†). Under high-temperature conditions, precursor molecules undergo polymerization and dehydration, forming complex polymer/carbon hybrid structure of CDs, where molecular fluorophores may be covalently attached to CDs.[10] Unfortunately, the structural complexity of CDs makes it difficult to build exact model structures, thus forcing researchers to reach for *ad hoc* models.[55–59] Our *ad hoc* model represents the polymeric **CND** model synthesized in the conditions before reaching full-carbonization, where small fluorophores may still dominate the optical properties of **CNDs**.[57,60,61] The MD simulations revealed that the system self-assembled into the **CND** shaped particle within the simulation time (Fig. S17 Sections b–f, ESI†), with the average radius of gyration 1.0 nm (Fig. S18a, ESI†), thus the estimated hydrodynamic radius of this model shall be around 2.5 nm[62] (see the note in the ESI†). This **CND** model was observed to be stabilized not only by hydrogen-bond formation (Fig. S18b, ESI†), but especially through the stacking of the 12 IPCA molecules (5-oxo-1,2,3,5-tetrahydroimidazo-[1,2-α]-pyridine-7-carboxylic acid), which are covalently embedded within the **CND** (Fig. S19, ESI†).

Subsequently, a quantum mechanics/molecular mechanics (QM/MM) approach based on tight-binding DFT[63,64] and TD-ωB97XD/6-31G(d) methods were benchmarked to calculate UV-vis spectra in DMSO (Table S1 and Fig. S21 and S22, ESI†). The absorption spectra for **CND** shows that the most intense and lowest-energy transition S_1 (357 nm, f = 0.27, Fig. 5) is in excellent agreement with the experimental λ_{Abs} = 357 nm value reported in Table 2. Motivated by these results, the **CND** model was chemically functionalized with one azo derivative at different sites at the surface of the **CND** (Table S2, ESI†). The most thermodynamically stable constitutional isomer of **CND–azo** was selected for TDDFT computations (Fig. S24, ESI†).

Specifically, **CND–*p*-Azo** was selected as a representative example for the analysis of the TDDFT results, while calculated spectra and electron transition schemes for both *para* and *meta* conformers of *cis*/*trans* azo compounds, and the respective **CND–azo** hybrids, are presented in Fig. S25–S30 (ESI†). To confirm that the wB97xD/6-31G(d) functional and basis set combination used is a good choice to reproduce the experimental spectra, we performed benchmark experiments (see ESI† for details). The lowest-energy electronic transitions in **CND–*p*-Azo** incorporating the *trans* isomer of the azo fragment are illustrated in Fig. 5. The first strong peak obtained is attributed to the S_1 n–π* transition at 513 nm, localized on the azo fragment, **CND–*p*-Azo**** (where the * indicates the moiety that is excited). The second peak/shoulder relates to the S_2 π–π* transition at 397 nm, exhibiting a strong CT character, from the **CND** to the Azo moiety (**CNDs+–*p*-Azo**$^-$). Furthermore, the calculated maximum of absorption intensity at 336 nm (f = 1.08) is in very good agreement with the experimental value of 349 nm. This peak is assigned to the π–π* transition S_3 localized on the azo moiety, **CND–*p*-Azo****, which is analogous to S_2, although they differ in their orbital contributions. The π–π* transitions S_4 and S_5 are localized excitations on the nanodot fragment, **CND***–***p*-Azo**, which are blue shifted by at least 26 nm compared with the peak of 357 nm in pristine **CND**. Furthermore, the system is prone to CT events, since either S_4 or S_5 may undergo internal conversion to CT S_2 state. The corresponding CT reactions **CND***–***p*-Azo** → **CND**$^+$**–*p*-Azo**$^-$ are associated with favorable driving forces (0.6 eV for S_4 → S_2 and 0.8 eV for S_5 → S_2, see Fig. 5), assuming neglecting entropic effects, which is valid under the Franck–Condon approximation. In summary, considering **CND–azo** incorporating the azo fragment in *para*/*meta* and *cis*/*trans* configurations, electronic transitions in the UV region

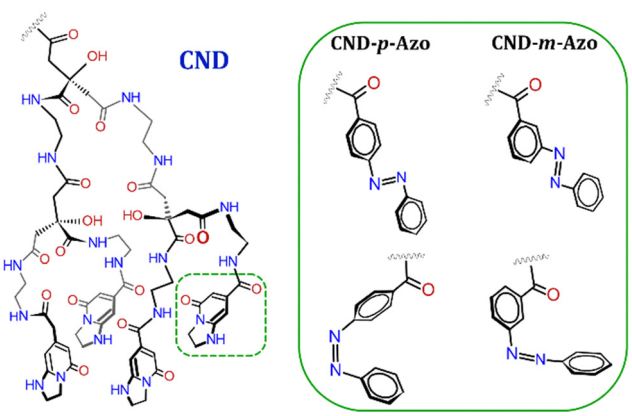

Fig. 4 Structures of the **CND–azo** hybrids used in the computation.

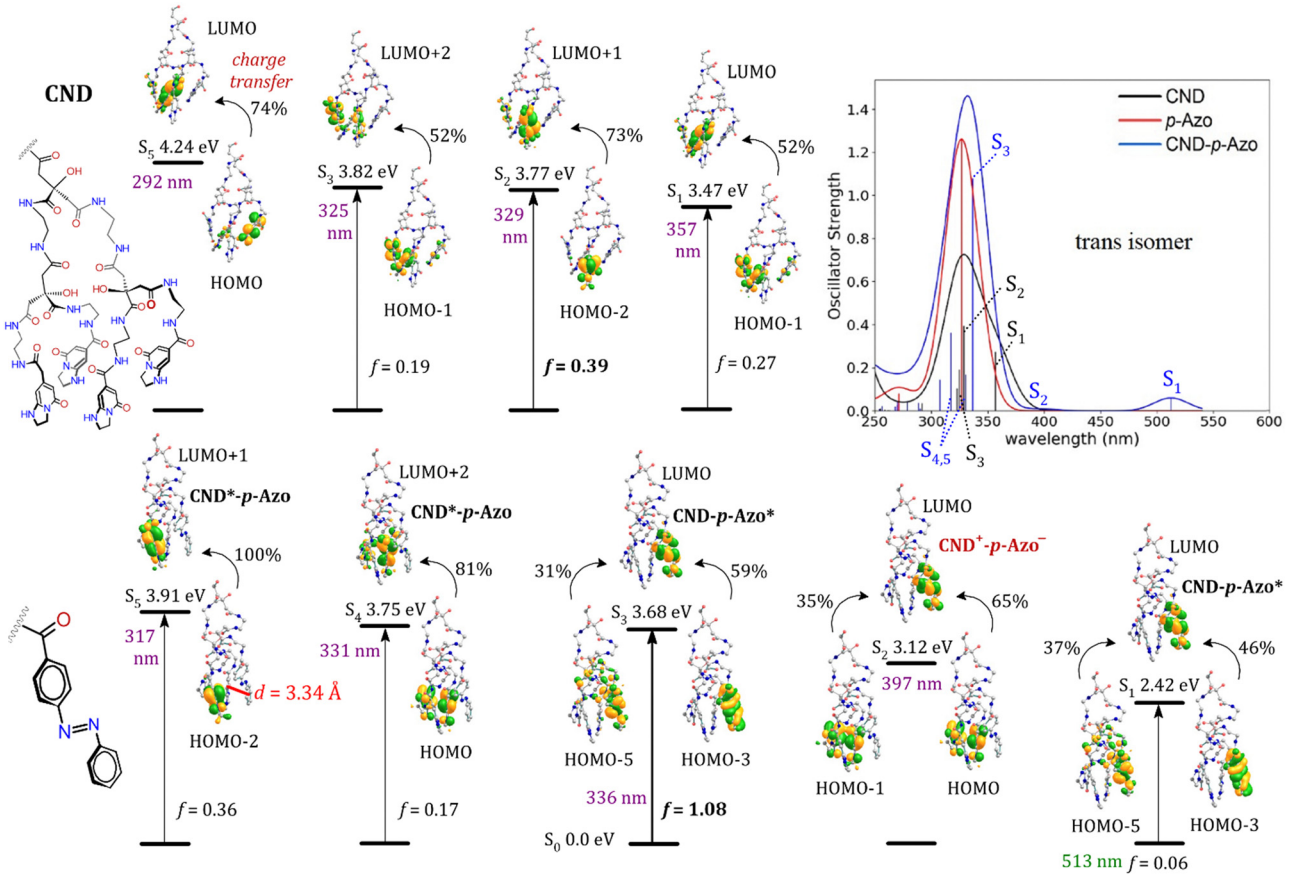

Fig. 5 The lowest-energy electron transitions in the **CND** (top) and **CND–*p*-Azo** (bottom, *f* = oscillator strength, % of molecular-orbital contributions). The azo moiety is in the *trans* configuration. Only the fragment simulated at the TDFFT level is illustrated for the sake of clarity. The calculated spectrum is also illustrated.

occur in both fragments (**CND–azo*** and **CND*–Azo**) for both *para* and *meta* conformers (see Fig. 5 and Fig. S30, respectively, ESI†) in the *trans* azo isomer. Conversely, for the *cis* isomer, excitations are primarily characterized by **CND*–Azo** in the UV region (Fig. S26 and S27, ESI†). We observed that the spectra of the hybrids incorporating the *trans* configuration of the azo moiety exhibit closer alignment with the experimental evidence (Fig. S28, ESI†). These findings suggest that the *trans* isomer of azo in the **CND–azo** hybrid is predominant in the electron transitions. In this regard, experiments determined that a wavelength of 340 nm induces the conversion to the *cis* isomer in the hybrids (Fig. 7). We additionally examined CT excitation energies (ω) in the hybrids, which shifted by 72 nm and 65 nm for *trans* **CND–*p*-Azo** and **CND–*m*-Azo** compared with the *cis* conformer, respectively (see Table 3). Nonetheless, CT excited states can be also accessed in the hybrids containing the *cis* isomer, albeit with smaller values. In this context, this *cis*/*trans* CT activity may be envisioned for use in photoswitching (on/off), data storage (0, 1), or molecular transistors (*gate* open/close).

Similar trends are observed for the incorporation of a molecular spacer, **CND–*m*-Gly-Azo** (Fig. S31–S35, ESI†). Nonetheless, the flexibility provided by the molecular spacer either induces (when $d < 4$ Å) or inhibits (when $d > 6$ Å) the formation of CT states (presented in Table 3). However, the flexibility of the molecular spacer allows access to various structural configurations, indicating that CT states are not strictly inhibited.

Further, functionalization of the **CND** did not significantly change the emission maximum, as observed in the excitation–emission maps and excitation spectra of the **CND** and the hybrids (Fig. S37 and S38, ESI†). This aligns with the computational assumption put forth in this study and in our previous investigation, where an aggregated molecular fluorophore, IPCA, was identified as the primary PL source of the **CNDs**.[10,16]

Table 3 Charge transfer excitation energies (ω), Hirshfeld charges (q) in azo and **CND** along with the distance (d)[a] between these fragments

Hybrid	ω [*nm* (eV)]	q_{azo} (e)	q**CND** (e)	d (Å)
trans **CND–*p*-Azo**	397 (3.12)	−0.72	+0.72	3.34
trans **CND–*m*-Azo**	375 (3.30)	−0.64	+0.64	3.44
trans **CND–*m*-Gly-Azo**	374 (3.31)	−0.76	+0.76	3.41
trans **CND–*m*-Gly-Azo**	Inhibited			7.95
cis **CND–*p*-Azo**	325 (3.81)	−0.74	+0.74	3.24
cis **CND–*m*-Azo**	310 (4.00)	−0.85	+0.85	3.90
cis **CND–*m*-Gly-Azo**	351 (3.53)	−0.85	+0.85	2.86
cis **CND–*m*-Gly-Azo**	Inhibited			17.02

[a] d stands for the distance between the phenyl centroid in *trans*- or the N=N group in *cis*-azo and the closest centroid of IPCA in the **CND**.

It is notable that the molecular fluorophores present in the **CND** are not directly covalently linked with the azos; rather, they interact through space. Moreover, a through-bond mechanism appears to be unlikely for the lowest excited states, as the excitation energies are localized on the individual units, as illustrated in Fig. 5.

Accordingly, a through-space mechanism, such as Förster resonance energy transfer (FRET) or electron transfer, is a viable option, given the close proximity of the units (see Table 3).[65–68] FRET relies on a dipole–dipole interaction, where the resonance between the donor's emission and the acceptor's absorbance and the relative orientation of their transition dipole moments plays a crucial role.[69] In contrast, electron transfer requires a substantial overlap between the donor and acceptor orbitals, a prerequisite that is plausible based on our computed model.[70,71] The potential of our synthesized hybrids to undergo both charge transfer and FRET suggests that quenching efficiency may be influenced by both mechanisms. As shown in Fig. 3, the **CND** emission strongly overlaps with the n–π* absorbance of the azo moieties, making a FRET from **CND** to the azo moieties possible. This was further confirmed by overlap integral calculations, which were used to determine the critical Förster radius (R_0) (see ESI† for details). The R_0 values vary slightly among the hybrids, averaging around 2.1 nm. Using these values and the distances listed in Table 3, FRET efficiencies were calculated, revealing a near-complete (99.9%) transfer efficiency for all three hybrids. This high efficiency results from the short **CND**-to-azo distance, which at 0.33 nm is well below the Förster radius.

However, the PLQY measurements indicate that this high efficiency is valid only for **CND–*m*-Gly-Azo**, as the other hybrids still exhibit a significant amount of **CND** fluorescence. To account for these differences, the quenching efficiency was determined using PLQY, since both FRET and electron transfer typically reduce the fluorescence quantum yield and lifetime of the donor. The resulting quenching efficiencies were 51% for **CND–*m*-Azo**, 70% for **CND–*p*-Azo**, and 97% for **CND–*m*-Gly-Azo**. Notably, quenching efficiency depends on the acceptor concentration within the system. Due to the undefined structural configuration of the hybrids and the unknown number of azo moieties per **CND**, accurately quantifying the relative contributions of different quenching processes is not possible.[67]

The elevated quenching efficiencies should also correspond to reduced fluorescence lifetimes of the **CND** moiety. To verify this, the fluorescence lifetimes of the pure **CND** and the hybrids were measured using TCSPC. All four systems exhibited three distinct fluorescence lifetimes, reflecting the complex surface structure of the **CNDs**. For the simplicity, these lifetimes were combined into an amplitude-weighted average lifetime. As expected, the pure **CND** holds with 5.70 ns the longest average fluorescence lifetime, followed by 3.60 ns and 3.45 ns for **CND–*p*-Azo** and **CND–*m*-Azo**, respectively. In contrast, with only 2.24 ns, the linker in **CND–*m*-Gly-Azo** clearly leads to the shortest fluorescence lifetime (Fig. 6 and Table S3, ESI†). While these lifetimes can also be used to estimate the quenching efficiencies of the hybrids, the obtained values are less reliable

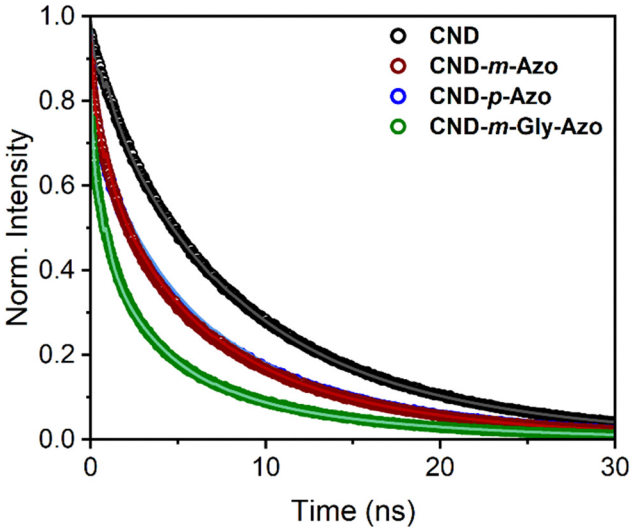

Fig. 6 Decay curves of the fluorescence transients recorded with TCSPC. While the raw data are shown as circles, the respective fits consist of solid curves in a slightly darker colour.

(see ESI† discussion for more details). The superior quenching efficiency of **CND–*m*-Gly-Azo**, in comparison to the hybrids that lack a linker, can be attributed to its higher density of functionalization. A greater density of azo moieties on the **CND** surface increases the probability of quenching. Additionally, our computational study demonstrated that the larger spacer in **CND–*m*-Gly-Azo** enhances flexibility and brings the azo units into closer proximity to the **CND**, further facilitating charge transfer processes.

To confirm the retained photoswitching properties of the azos after covalent bonding to **CNDs**, the hybrids and bare azos were irradiated with a 325 nm LED for two minutes, followed by a 448 nm LED irradiation for 30 seconds, followed by measurement of the absorption spectra before and after each illumination (Fig. S39, ESI†). Among the hybrids, **CND–*m*-Azo** exhibited the smallest absorbance change upon *trans-cis* isomerization, whereas **CND–*m*-Gly-Azo** showed the largest, consistent with their respective degrees of functionalization. Among the pristine azos, the ***p*-Azo** displayed the smallest decrease in absorbance when irradiated with the 325 nm LED (Fig. S39, ESI†). However, the **CND–*p*-Azo**, demonstrated a greater change in absorbance than the **CND–*m*-Azo**, indicating that its 1.1% higher degree of functionalization outweighs the smaller change in absorbance observed in pure ***p*-Azo**. Additionally, pure azos exhibited greater changes in absorbance compared to hybrids, likely due to the significant contribution of the **CND** component to overall absorbance. The PL response to photoswitching indicated no significant reversible change in PLQY from the *trans* to the *cis*-isomers of the covalently linked azos. However, a slight decrease in PL intensity post-illumination prompted an investigation into fatigue resistance across multiple photoswitching cycles and associated PL properties (Fig. 7A–C). The selection of wavelengths was based on the absorption maxima of the hybrids, specifically 340 nm and 448 nm. The 340 nm wavelength was chosen to balance sufficient excitation energy while

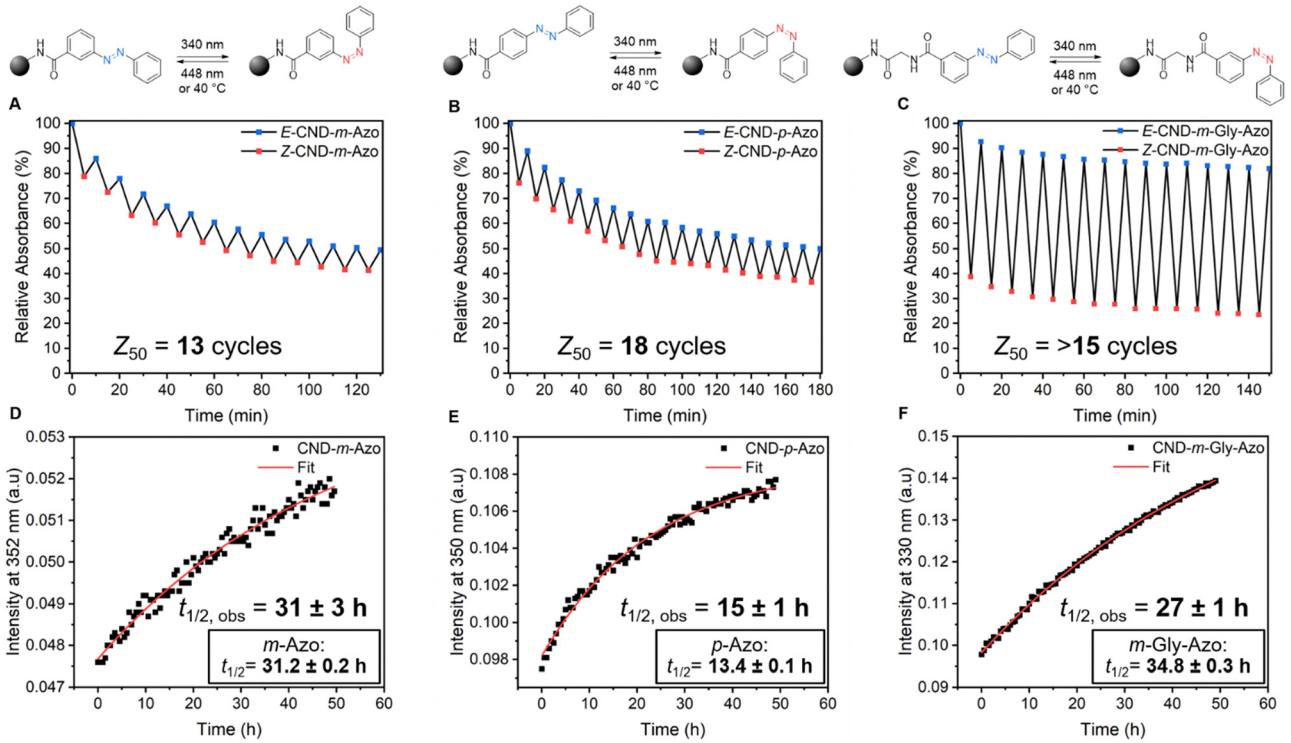

Fig. 7 **Top panel:** Schematic illustration of the azo-functionalized **CNDs** (black spheres), showing the photoinduced *trans*-to-*cis* conversion under 340 nm irradiation and subsequent reversion to the *trans*-isomer *via* 448 nm exposure or thermal isomerization at 40 °C. **Middle panel:** Fatigue resistance of **CND–azo** hybrids over multiple photoisomerization cycles using alternating 340 nm and 448 nm irradiation. (A) **CND–*m*-Azo** retains 50% of its initial absorbance at 350 nm for 13 *trans*–*cis*–*trans* cycles. (B) **CND–*p*-Azo** shows stability for 18 cycles at 349 nm. (C) **CND–*m*-Gly-Azo** maintains more than 50% absorbance at 329 nm for more than 15 cycles. **Bottom panel:** Thermal *cis*-to-*trans* isomerization kinetics of the hybrids at 40 °C over 50 h. Pristine azo half-lives are included for comparison (see ESI† for details). (D–F) Evolution of the absorbance at 352 nm (**CND–*m*-Azo**), 350 nm (**CND–*p*-Azo**), and 330 nm (**CND–*m*-Gly-Azo**) during thermal reversion. Single-exponential fits were used to determine half-lives. **Note:** Graphs D and E are normalized to their respective isosbestic points at 363 nm and 397 nm respectively, as agglomeration accurse over the time scale of the kinetic experiment. Due to the higher loading of azo in the **CND–*m*-Gly-Azo** hybrid, no spectra processing was necessary (see ESI† for details).

minimizing photodegradation. Each hybrid was irradiated for five minutes at these wavelengths to achieve the photostationary state (PSS) of the respective isomer (see Fig. S40, ESI†). **CND–*m*-Azo** underwent 13 *trans–cis–trans* cycles before reaching 50% of its original absorbance (Z_{50}).

In contrast, **CND–*p*-Azo** maintained 50% of its original absorbance over 18 cycles, demonstrating greater stability than **CND–*m*-Azo**. **CND–*m*-Gly-Azo** exhibited an 18% decrease in absorbance after 15 cycles, indicating it is the most durable hybrid produced. Fig. S41 (ESI†) shows the PL spectra following fatigue resistance tests, showing a similar decline in PL intensity corresponding to absorbance degradation. This suggests that the switching properties of the azos on the **CND** surface remain unaltered, while contributions from absorption and emission of the **CNDs** diminish. This hypothesis is supported by fatigue resistance measurements conducted under identical conditions with the pure Azos (Fig. S42, ESI†). After 120 minutes of light exposure, no significant drop in absorbance can be observed. Azos exhibit high fatigue resistance due to minimal occurrence of side reactions during photoisomerization. The increased fatigue resistance of the **CND–*m*-Gly-Azo** hybrid may be due to a higher azo coverage of the **CND** surface by the introduction of a glycine spacer. In classical organic chemistry, undesired reactions involving a reactive intermediate often lead to the generation of side-products. By offering an inert environment for these intermediates, confinement can serve as a method to reduce side-product formation and enhance the fatigue resistance.[72] Additionally, we assessed the thermal half-life of the *cis*-isomer of the hybrids at 40 °C in DMSO (Fig. 7D–F). A schematic representation of the azos on the **CND** surface, which is switched between *trans*- and *cis*-isomers *via* light or heat, is shown in the top panel of Fig. 7. Fig. S43–S48 (ESI†) display UV-vis spectra illustrating thermal conversion from *cis*- to *trans*-isomer alongside single exponential fits against time to determine the thermal half-lives (Table S6, ESI†). The hybrids tend to agglomerate during the 50-hour thermal *cis*-to-*trans* isomerization, which is potentially distorting the data. In order to compensate that, we normalized the absorption spectra of the **CND–*m*-Azo** and **CND–*p*-Azo** to the isosbestic points (see ESI† for details).

The **CND–*m*-Azo** variant exhibits minimal variation in half-life compared to pure ***m*-Azo**, while the **CND–*m*-Gly-Azo** hybrid displays a reduced half-life relative to ***m*-Gly-Azo**. For the *meta*-linked hybrids, it is assumed that they behave electronically independently from the **CNDs**. The observed differences can be attributed to steric effects and the degree of functionalization,

resulting in comparable or shorter half-lives than pure azos. Further systematic studies are required to quantify these contributions. In contrast, the **CND–*p*-Azo** demonstrates an increased half-life compared to ***p*-Azo**, suggesting that the electronic properties of the hybrid – modulated by the exchange of the carboxylic acid for an amide – can also play a role in altering the half-life. Furthermore, the precise chemical background of the functionalization employed, namely the amine on the **CND** side, has the potential to exert different electronic influences, given the lack of knowledge regarding the **CND** structure.

A comparison of the obtained results with other carbon allotropes functionalized with azos in the literature reveals that the influence of **CNDs** on the switching properties of the azos is relatively weak. In the case of fullerene, a publication by Shirai *et al.*[73] in 2008 demonstrated that direct conjugation of fullerene with an azo led to reduced photoisomerization yields, suggesting an efficient electronic energy transfer between the azo and fullerene. However, when fullerene and azo were electronically separated *via* a spacer, this effect was not observed. In our case, this further supports the hypothesis that the chemical nature of **CNDs** leads to electronic separation of the molecular fluorophores on **CNDs** and azo in all three of our investigated hybrids. Indeed, TDDFT results for **CND–*m*-Gly-Azo** revealed that the formation of CT states depends upon the distance between **CND** and azo, as previously concluded. In 2013, Feng *et al.*[74] introduced a reduced graphene oxide (RGO)-azo hybrid for long-term solar thermal storage. By achieving high packing densities and incorporating additional *ortho* and *para* functionalization of the azos with moieties that facilitate the formation of H-bonds, they successfully attained extended half-lives of the *cis*-isomer. The quasi-spherical and amorphous character of **CNDs** prevents the establishment of a repeating structure, allowing the azo units to orient in various directions without forming ordered configurations as seen on a RGO surface. Furthermore, the limited amount of azo present on the surface likely suppresses interactions between different azo units on a single **CND**.

Conclusions

In this study, three distinct **CND–azo** hybrids were synthesized, featuring either *meta*- or *para*-linkages as well as an additional glycine spacer. These hybrids exhibit both photoswitching capability and emissive properties, allowing them to be sensed and optically stimulated in the same system. The incorporation of the glycine spacer resulted in an increase in fatigue resistance, likely due to the formation of an inert environment around the **CND**. Furthermore, a reduction in the half-life of the *cis* isomer was observed in the case of the hybrid with the glycine spacer. In contrast, the two hybrids without the spacer exhibited similar half-lives compared to their pristine azo counterparts. This shorter half-life renders the system useful in optical switches due to their fast response to external stimuli. Furthermore, investigations using TDDFT methods were performed to gain deeper insights into the experimental UV-vis absorption spectra and CT properties of the **CND–azo** hybrids. This approach enhanced our understanding of the influence of isomer configuration on electronic transitions, and it provided valuable guidance for the development of potential applications. The results demonstrate that *trans*-azo in **CND–azo** hybrids significantly stabilizes the LUMO energy, leading to enhanced CT activity compared to the *cis* counterpart. Specifically, *trans* isomers exhibit a lower CT excitation energy and more favorable driving forces for CT reactions, making them more effective for applications requiring efficient electron transfer. In contrast, *cis* isomers undergo CT processes but with reduced driving forces. This difference underscores the potential of functionalized **CND–azo** hybrids for use in photoswitches, data storage, and molecular transistors where CT is critical. The addition of molecular spacers, such as in **CND–*m*-Gly-Azo**, further illustrates that spacer flexibility influences the formation of CT states. Specifically, spacer distances greater than 6 Å inhibit CT states, while shorter distances can promote them, emphasizing the need for careful spacer design to optimize electronic properties. Lastly, the total emission quenching efficiencies for the hybrids were calculated from fluorescence lifetimes obtained with TCSPC measurements. The fluorescence lifetimes of the hybrids were observed to be shorter than those of the pristine **CND**, with the shortest lifetime noted for the **CND–*m*-Gly-Azo** hybrid. This is attributed to the higher concentration of azo groups present on the surface, as well as the higher flexibility of the spacer, which promotes CT processes. Overall, these findings highlight the potential of azo-functionalized **CND** hybrids in developing advanced light-responsive systems. This represents an intriguing point of departure for the design of novel scaffolds that can be integrated into devices, sensors/actuators, or living cells that are remotely controlled through light irradiation.

Author contributions

P. P. D.: writing original draft, conceptualization, investigation; D. S.: writing original draft, conceptualization, investigation; Y. A.-S.: investigation, conceptualization; J. P. M.: writing original draft, conceptualization, investigation in the computational section; M. L.: writing original draft, investigation, computations; J. H.: investigation; J. G.: writing – review & editing, conceptualization; E. M.: investigation, supervision, resources; B. M. S.: supervision, resources; M. S.: supervision, resources; S. O.: writing – review & editing, conceptualization, resources; J. W.: supervision, resources; H. A. W.: writing – review & editing, conceptualization, project administration; T. G.: writing – review & editing, conceptualization, project administration.

Data availability

The data supporting this article have been included as part of the ESI.†

Conflicts of interest

The authors declare no conflict of interest.

Acknowledgements

We thank the financial support of the DFG and of the National Science Center, Poland through the joint project ''Low-Dimensional Nano-Architectures for Light Emission and Light-to-Electricity Conversion'' (LOW-LIGHT, grant no. UMO/2020/39/I/ST4/01446). D. S. thanks the European and Hessian Government for funding the ''Innovationslabor Prozessdiagnostik'' (EFRE 21031934). J. P. M. acknowledges the funding of a post-doctoral contract by the LOW-LIGHT grant. T. G. acknowledges the European Research Council for the project JANUS BI (grant agreement no. [101041229]). M. L. acknowledges that this article has been produced with the financial support of the European Union under the REFRESH – Research Excellence For Region Sustainability and High-tech Industries project number CZ.10.03.01/00/22_003/0000048 *via* the Operational Programme Just Transition. This work was supported by the Ministry of Education, Youth and Sports of the Czech Republic through the e-INFRA CZ (ID: 90254). J. W. gratefully acknowledges the European Union for funding the TCSPC laser system through the European Regional Development Fund as part of the Union's response to the COVID-19 pandemic – REACT-EU, IWB-EFRE-Programm Hessen, \#20008794. The authors thank Heike Hausmann (JLU, Giessen) for performing the NMR ^{1}H and ^{13}C spectra and Pascal Schweitzer (JLU, Giessen) for the support with the AFM measurements.

References

1 G. M. Paternò, G. Bondelli and G. Lanzani, *Bioelectricity*, 2021, **3**, 136–142.
2 T. L. Doane and C. Burda, *Chem. Soc. Rev.*, 2012, **41**, 2885.
3 T. C. de Souza-Guerreiro, G. Bondelli, I. Grobas, S. Donini, V. Sesti, C. Bertarelli, G. Lanzani, M. Asally and G. M. Paternò, *Adv. Sci.*, 2023, **10**, 2205007.
4 B. Mavroidi, A. Kaminari, E. Sakellis, Z. Sideratou and D. Tsiourvas, *Pharmaceuticals*, 2023, **16**, 833.
5 S. Zhang, C. Xiao, H. He, Z. Xu, B. Wang, X. Chen, C. Li, B. Jiang and Y. Liu, *Environ. Sci.: Nano*, 2020, **7**, 880–890.
6 M. Döbbelin, A. Ciesielski, S. Haar, S. Osella, M. Bruna, A. Minoia, L. Grisanti, T. Mosciatti, F. Richard, E. A. Prasetyanto, L. De Cola, V. Palermo, R. Mazzaro, V. Morandi, R. Lazzaroni, A. C. Ferrari, D. Beljonne and P. Samorì, *Nat. Commun.*, 2016, **7**, 11090.
7 D. Niedzialek, I. Duchemin, T. B. De Queiroz, S. Osella, A. Rao, R. Friend, X. Blase, S. Kümmel and D. Beljonne, *Adv. Funct. Mater.*, 2015, **25**, 1972–1984.
8 S. Osella, M. Wang, E. Menna and T. Gatti, *Opt. Mater. X*, 2021, **12**, 100100.
9 A. M. Ross, S. Osella, V. R. Policht, M. Zheng, M. Maggini, F. Marangi, G. Cerullo, T. Gatti and F. Scotognella, *J. Phys. Chem. C*, 2022, **126**, 3569–3581.
10 M. Langer, L. Zdražil, M. Medveď and M. Otyepka, *Nanoscale*, 2023, **15**, 4022–4032.
11 A. Banger, S. Gautam, S. Jadoun, N. K. Jangid, A. Srivastava, I. N. Pulidindi, J. Dwivedi and M. Srivastava, *Catalysts*, 2023, **13**, 858.
12 S. N. Baker and G. A. Baker, *Angew. Chem., Int. Ed.*, 2010, **49**, 6726–6744.
13 Y.-P. Sun, B. Zhou, Y. Lin, W. Wang, K. A. S. Fernando, P. Pathak, M. J. Meziani, B. A. Harruff, X. Wang, H. Wang, P. G. Luo, H. Yang, M. E. Kose, B. Chen, L. M. Veca and S.-Y. Xie, *J. Am. Chem. Soc.*, 2006, **128**, 7756–7757.
14 F. Arcudi, L. Đorđević and M. Prato, *Acc. Chem. Res.*, 2019, **52**, 2070–2079.
15 F. Rigodanza, M. Burian, F. Arcudi, L. Đorđević, H. Amenitsch and M. Prato, *Nat. Commun.*, 2021, **12**, 2640.
16 P. P. Debes, M. Langer, M. Pagel, E. Menna, B. Smarsly, S. Osella, J. Gallego and T. Gatti, *ChemNanoMat*, 2024, **10**, e202300471.
17 Y. Park, J. Yoo, B. Lim, W. Kwon and S.-W. Rhee, *J. Mater. Chem. A*, 2016, **4**, 11582–11603.
18 F. Arcudi, V. Strauss, L. Đorđević, A. Cadranel, D. M. Guldi and M. Prato, *Angew. Chem.*, 2017, **129**, 12265–12269.
19 B. Liao, P. Long, B. He, S. Yi, B. Ou, S. Shen and J. Chen, *J. Mater. Chem. C*, 2013, **1**, 3716.
20 X. Zhang, L. Hou and P. Samorì, *Nat. Commun.*, 2016, **7**, 11118.
21 K. Nakatani, J. Piard, P. Yu and R. Métivier, in *Photochromic Materials: Preparation, Properties and Applications*, ed. H. Tian and J. Zhang, Wiley-VCH Verlag GmbH & Co. KGaA, Weinheim, Germany, 2016, pp. 1–45.
22 T. Nägele, R. Hoche, W. Zinth and J. Wachtveitl, *Chem. Phys. Lett.*, 1997, **272**, 489–495.
23 J. L. Oudar, *J. Chem. Phys.*, 1977, **67**, 446–457.
24 M. J. Moran, M. Magrini, D. M. Walba and I. Aprahamian, *J. Am. Chem. Soc.*, 2018, **140**, 13623–13627.
25 L. Hegedüsová, N. Blaise, L. F. Pašteka, Š. Budzák, M. Medveď, J. Filo, B. Mravec, C. Slavov, J. Wachtveitl, A. M. Grabarz and M. Cigáň, *Chem. – Eur. J.*, 2024, **30**, e202303509.
26 B. Mravec, Š. Budzák, M. Medved', L. F. Pašteka, C. Slavov, T. Saßmannshausen, J. Wachtveitl, J. Kožíšek, L. Hegedüsová, J. Filo and M. Cigáň, *J. Org. Chem.*, 2021, **86**, 11633–11646.
27 J. C. Tobin, A. F. Hegarty and F. L. Scott, *J. Chem. Soc. B Phys. Org.*, 1971, 2198–2202.
28 A. I. A. Soliman, M. Sayed, M. M. Elshanawany, O. Younis, M. Ahmed, A. M. Kamal El-Dean, A.-M. A. Abdel-Wahab, J. Wachtveitl, M. Braun, P. Fatehi and M. S. Tolba, *ACS Omega*, 2022, **7**, 10178–10186.
29 Z. Wang, R. Losantos, D. Sampedro, M. Morikawa, K. Börjesson, N. Kimizuka and K. Moth-Poulsen, *J. Mater. Chem. A*, 2019, **7**, 15042–15047.
30 L. Dong, Y. Feng, L. Wang and W. Feng, *Chem. Soc. Rev.*, 2018, **47**, 7339–7368.
31 K. Kreger, P. Wolfer, H. Audorff, L. Kador, N. Stingelin-Stutzmann, P. Smith and H.-W. Schmidt, *J. Am. Chem. Soc.*, 2010, **132**, 509–516.

32 M. A. Gerkman and G. G. D. Han, *Joule*, 2020, **4**, 1621–1625.
33 Z. Wang, P. Erhart, T. Li, Z.-Y. Zhang, D. Sampedro, Z. Hu, H. A. Wegner, O. Brummel, J. Libuda, M. B. Nielsen and K. Moth-Poulsen, *Joule*, 2021, **5**, 3116–3136.
34 D. Schatz, M. E. Baumert, M. C. Kersten, F. M. Schneider, M. B. Nielsen, M. M. Hansmann and H. A. Wegner, *Angew. Chem., Int. Ed.*, 2024, **63**, e202405618.
35 K. Hüll, J. Morstein and D. Trauner, *Chem. Rev.*, 2018, **118**, 10710–10747.
36 M. O. Lenz, A. C. Woerner, C. Glaubitz and J. Wachtveitl, *Photochem. Photobiol.*, 2007, **83**, 226–231.
37 M. Liu, X. Yan, M. Hu, X. Chen, M. Zhang, B. Zheng, X. Hu, S. Shao and F. Huang, *Org. Lett.*, 2010, **12**, 2558–2561.
38 C. Averdunk, K. Hanke, D. Schatz and H. A. Wegner, *Acc. Chem. Res.*, 2024, **57**, 257–266.
39 Y. Norikane and N. Tamaoki, *Org. Lett.*, 2004, **6**, 2595–2598.
40 G. S. Hartley, *Nature*, 1937, **140**, 281.
41 E. Merino and M. Ribagorda, *Beilstein J. Org. Chem.*, 2012, **8**, 1071–1090.
42 D. Schulte-Frohlinde, *Ann. Chem.*, 1958, **612**, 138–152.
43 A. Goulet-Hanssens, C. Rietze, E. Titov, L. Abdullahu, L. Grubert, P. Saalfrank and S. Hecht, *Chem*, 2018, **4**, 1740–1755.
44 C. Slavov, C. Yang, L. Schweighauser, C. Boumrifak, A. Dreuw, H. A. Wegner and J. Wachtveitl, *Phys. Chem. Chem. Phys.*, 2016, **18**, 14795–14804.
45 S. Bellotto, R. Reuter, C. Heinis and H. A. Wegner, *J. Org. Chem.*, 2011, **76**, 9826–9834.
46 R. Reuter, N. Hostettler, M. Neuburger and H. A. Wegner, *Eur. J. Org. Chem.*, 2009, 5647–5652.
47 R. Ziessel, P. Stachelek, A. Harriman, G. J. Hedley, T. Roland, A. Ruseckas and I. D. W. Samuel, *J. Phys. Chem. A*, 2018, **122**, 4437–4447.
48 F. Raymo and M. Tomasulo, *Chem. Soc. Rev.*, 2005, **34**, 327–336.
49 I. J. Gomez, B. Arnaiz, M. Cacioppo, F. Arcudi and M. Prato, *J. Mater. Chem. B*, 2018, **6**, 5540–5548.
50 W. S. Price, *NMR Studies of Translational Motion: Principles and Applications*, Cambridge University Press, Cambridge, 2009.
51 S. Sarkar, S. Dinda, P. Choudhury and P. K. Das, *Soft Matter*, 2019, **15**, 2863–2875.
52 R. Luther and A. Nikolopulos, *Z. Physiol. Chem.*, 1913, **82U**, 361–384.
53 P. P. Debes, M. Pagel, S. Muntean, J. Hessling, B. M. Smarsly, M. Schönhoff and T. Gatti, *Photochem*, 2025, **5**, 1.
54 G. Filippini, F. Amato, C. Rosso, G. Ragazzon, A. Vega-Peñaloza, X. Companyó, L. Dell'Amico, M. Bonchio and M. Prato, *Chem*, 2020, **6**, 3022–3037.
55 M. Langer, T. Hrivnák, M. Medved and M. Otyepka, *J. Phys. Chem. C*, 2021, **125**, 12140–12148.
56 M. Langer, M. Paloncýová, M. Medved and M. Otyepka, *J. Phys. Chem. Lett.*, 2020, **11**, 8252–8258.
57 M. J. Krysmann, A. Kelarakis, P. Dallas and E. P. Giannelis, *J. Am. Chem. Soc.*, 2012, **134**, 747–750.
58 L. Vallan, E. P. Urriolabeitia, F. Ruipérez, J. M. Matxain, R. Canton-Vitoria, N. Tagmatarchis, A. M. Benito and W. K. Maser, *J. Am. Chem. Soc.*, 2018, **140**, 12862–12869.
59 X. Zhao, J. Wei, T. Song, Z. Wang, D. Yang, X. Zhang, F. Huo, Y. Zhang and H.-M. Xiong, *Chem. Eng. J.*, 2024, **481**, 148779.
60 C. Xia, S. Zhu, T. Feng, M. Yang and B. Yang, *Adv. Sci.*, 2019, **6**, 1901316.
61 F. Ehrat, S. Bhattacharyya, J. Schneider, A. Löf, R. Wyrwich, A. L. Rogach, J. K. Stolarczyk, A. S. Urban and J. Feldmann, *Nano Lett.*, 2017, **17**, 7710–7716.
62 C. M. Kok and A. Rudin, *Makromol. Chem., Rapid Commun.*, 1981, **2**, 655–659.
63 C. Bannwarth, E. Caldeweyher, S. Ehlert, A. Hansen, P. Pracht, J. Seibert, S. Spicher and S. Grimme, *WIREs Comput. Mol. Sci.*, 2021, **11**, e1493.
64 C. Bannwarth, S. Ehlert and S. Grimme, *J. Chem. Theory Comput.*, 2019, **15**, 1652–1671.
65 I. Yildiz, M. Tomasulo and F. M. Raymo, *Proc. Natl. Acad. Sci. U. S. A.*, 2006, **103**, 11457–11460.
66 M. Sykora, M. A. Petruska, J. Alstrum-Acevedo, I. Bezel, T. J. Meyer and V. I. Klimov, *J. Am. Chem. Soc.*, 2006, **128**, 9984–9985.
67 P. Moroz, Z. Jin, Y. Sugiyama, D. Lara, N. Razgoniaeva, M. Yang, N. Kholmicheva, D. Khon, H. Mattoussi and M. Zamkov, *ACS Nano*, 2018, **12**, 5657–5665.
68 M. H. Stewart, A. L. Huston, A. M. Scott, A. L. Efros, J. S. Melinger, K. B. Gemmill, S. A. Trammell, J. B. Blanco-Canosa, P. E. Dawson and I. L. Medintz, *ACS Nano*, 2012, **6**, 5330–5347.
69 D. W. Piston and G.-J. Kremers, *Trends Biochem. Sci.*, 2007, **32**, 407–414.
70 E. F. Valeev, V. Coropceanu, D. A. da Silva Filho, S. Salman and J.-L. Brédas, *J. Am. Chem. Soc.*, 2006, **128**, 9882–9886.
71 J. L. Brédas, J. P. Calbert, D. A. da Silva Filho and J. Cornil, *Proc. Natl. Acad. Sci. U. S. A.*, 2002, **99**, 5804–5809.
72 M. Canton, A. B. Grommet, L. Pesce, J. Gemen, S. Li, Y. Diskin-Posner, A. Credi, G. M. Pavan, J. Andréasson and R. Klajn, *J. Am. Chem. Soc.*, 2020, **142**, 14557–14565.
73 Y. Shirai, T. Sasaki, J. M. Guerrero, B.-C. Yu, P. Hodge and J. M. Tour, *ACS Nano*, 2008, **2**, 97–106.
74 Y. Feng, H. Liu, W. Luo, E. Liu, N. Zhao, K. Yoshino and W. Feng, *Sci. Rep.*, 2013, **3**, 3260.